


Seebeck and Nernst effects of pseudospin-1 fermions in the  $\alpha - T_3$  model under magnetic fieldsWenye Duan <sup>\*</sup>*School of Physics, East China University of Science and Technology, Shanghai 200237, China* (Received 20 February 2023; revised 2 October 2023; accepted 9 October 2023; published 23 October 2023)

We numerically study the Seebeck and Nernst effects of pseudospin-1 fermions in the  $\alpha - T_3$  model under magnetic fields by combining the nonequilibrium Green's function and the Landauer-Büttiker formalism with the Stréda formula. In the  $\alpha = 0$  limit under strong magnetic fields, our results are in good agreement with theoretical results of graphene. Distinguishing from the case of  $\alpha = 0$ , we find three characteristic features and discuss them in detail analytically for  $\alpha > 0$ : (i) The inverse of the peak height of the Seebeck coefficient is  $\frac{-e}{\ln 2k_B} [n_p + \text{sign}(n_p)\delta]$ , with  $\delta = 1/2$  for  $\alpha > 0$  while  $\delta = 0$  for  $\alpha = 0$ , where  $n_p$  denotes the  $n_p$ th peak near the Dirac point. We show that  $\delta$  is determined by the Hall plateau series. (ii) The highest peak of the Seebeck coefficient is much higher than other peaks. This highest peak is ascribed to the vanishing of the Hall conductivity due to the energy gap between the flat band and lowest Landau level. (iii) There exists a negative peak near the Dirac point. We relate this unique behavior to the vanishing of the Hall conductivity near the Dirac point and the isolated flat band. Meanwhile, the peak of the Nernst coefficient for  $\alpha = 0$  splits into double peaks by increasing  $\alpha$  and the height is enhanced. Additionally, the effects of temperatures, disorders, the strength of magnetic field, and edge patterns are also investigated. These findings provide theoretical foundation for future experimental studies on the thermoelectric properties based on the  $\alpha - T_3$  materials.

DOI: [10.1103/PhysRevB.108.155428](https://doi.org/10.1103/PhysRevB.108.155428)**I. INTRODUCTION**

After the experimental fabrication of graphene monolayer in 2004 [1], relativistic materials have attracted extensive attention due to their unique physical properties as well as promising potential applications, such as the surface states of topological insulators [2,3], Dirac, and Weyl semimetals [4]. At low energy, the relativistic materials are described effectively by Dirac-Weyl Hamiltonians with pseudospin-1/2 and have linear energy-momentum relations as particles in high-energy physics which are constrained by the Poincaré symmetry and the spin-statistics theorem. Recently, due to the less restrictive symmetries in condensed matter systems, more sophisticated low-energy fermionic excitations with general pseudospins- $S = 1, 3/2, 2, \dots$  were proposed in lattices with special space groups and point-symmetry groups [5]. These high pseudospin fermions have been studied widely, especially for pseudospin  $S = 1$  systems [6–9]. One of the remarkable features of pseudospin  $S = 1$  systems is the flat band which could be realized in the dice lattice, Lieb lattice, and kagome lattice [9]. On the other hand, the correlated insulator and superconductivity in twisted bilayer graphene rejuvenated the interest of condensed matter physicists to flat or nearly flat bands [10,11]. As an adjustment of the dice lattice, the  $\alpha - T_3$  model provides an excellent platform to study both the pseudospin-1/2 and pseudospin-1 quasiparticles in a single model by varying the structure parameter  $\alpha$  which is associated with a continuously variable Berry phase [12].

As illustrated in Fig. 1(a), the  $\alpha - T_3$  lattice has three atomic sites per unit cell ( $A$ ,  $B$ , and  $C$ ). The rim sites  $A$  and  $B$  form the graphene-type honeycomb lattice, and an additional hub site  $C$  is at the center of the hexagon. The hopping amplitudes of  $A - B$  and  $B - C$  sites are  $t \cos \varphi$  and  $t \sin \varphi$ , respectively. The structure parameter  $\alpha = \tan \varphi$  is the ratio between  $B - C$  and  $A - B$  hopping amplitudes, and the hopping between  $A$  and  $C$  sites is forbidden. By varying the structure parameter  $\alpha$  continuously, this  $\alpha - T_3$  lattice can be modulated between graphene ( $\alpha = 0$ ) and the dice lattice ( $\alpha = 1$ ), continuously. As shown in Fig. 1(b), the low-energy band structure of the  $\alpha - T_3$  model is comprised of a linear Dirac cone and an additional flat band at the band center. Experimentally, the pseudospin-1 systems and  $\alpha - T_3$  model have been proposed to be realized in various achievable systems, such as trilayers of the face-centred cubic lattice in the [111] direction (for instance,  $\text{SrTiO}_3/\text{SrIrO}_3/\text{SrTiO}_3$ ) [7,13] and cold atoms confined to an optical [12,14,15]. Recently,  $\text{Hg}_{1-x}\text{Cd}_x\text{Te}$  quantum wells at a critical doping have been reported to map onto the  $\alpha - T_3$  model with  $\alpha = 1/\sqrt{3}$  [16,17].

Due to the unique band structure with a flat band and the  $\alpha$ -dependent Berry phase, the  $\alpha - T_3$  model exhibits unusual physical properties such as orbital susceptibility [12], super-Klein tunneling [18–20], the super Andreev reflection [21–23], linear and nonlinear optical response [8,24,25], dc conductivity [26–28], unique topological phases [13,29–32], Zitterbewegung [33], and Ruderman-Kittel-Kasuya-Yosida interaction [34,35]. Furthermore, a series of investigations has exploited the Floquet irradiated  $\alpha - T_3$  lattices [30,36–40]. Accordingly, valley-dependent transport properties have been explored [41–46], making the  $\alpha - T_3$  lattice promising for potential valleytronics applications. Especially in the

<sup>\*</sup>duanwy@pku.edu.cn

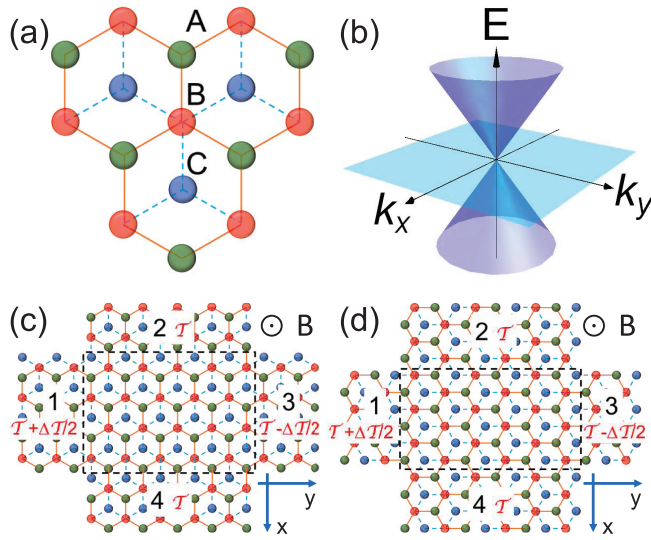


FIG. 1. (a) The lattice structure of the  $\alpha - T_3$  model, where  $A$  (green circle),  $B$  (red circle), and  $C$  (blue circle) represent the three sublattices. The hopping energy of  $A - B$  (orange solid line) is  $t \cos \varphi$  and of  $B - C$  (dashed blue line) is  $t \sin \varphi$ . (b) The low-energy band structure of the  $\alpha - T_3$  model at a single valley. (c), (d) Schematic diagrams for the four-terminal  $\alpha - T_3$  devices with zigzag and armchair edges of the lead-1,3 and the central region, respectively. The dashed black rectangle denotes the central scattering region.

presence of external magnetic fields, the unconventional quantum Hall effects [24,46–50] and magneto-optical conductivity [8,17,24,51–53] have been investigated extensively. Moreover, studies have also been extended to include additional mass terms [20,48,49,54–60] and strain variations [44,61] in  $\alpha - T_3$  lattices. The enhancement of thermoelectric properties of a two-terminal  $\alpha - T_3$  nanoribbon in the absence of magnetic field was recently reported [62]. However, studies on the Seebeck and Nernst effects of pseudospin-1 fermions in the  $\alpha - T_3$  model under magnetic fields are still lacking. In recent years, the Seebeck and Nernst coefficients of graphene under magnetic fields have been widely investigated both experimentally and theoretically [63–69]. Because of their sensitivity to the ambipolar behavior of relativistic excitations, the magnetothermoelectric measurements provide additional characteristics of graphene, which complement the inadequacy of conductivity measurements. In comparison with graphene, the Landau levels (LLs) of the  $\alpha - T_3$  model show spectral features [24]. Therefore, it is highly desirable to investigate how the Seebeck and Nernst coefficients change with  $\alpha$  varying from 0 to 1 under a perpendicular magnetic field. Furthermore, it is interesting to learn the effects of temperatures, the strength of magnetic fields, and disorders.

In this paper, we study the Seebeck coefficient  $S_{xx}$  and Nernst coefficient  $S_{xy}$  numerically by combining the nonequilibrium Green's function and the Landauer-Büttiker formalism with the Stréda formula in four-terminal  $\alpha - T_3$  devices under perpendicular magnetic fields. We perform an extensive study of their dependence on the structure parameter  $\alpha$ , temperatures, the strength of disorders, the strength of magnetic fields, and edge patterns. In the limit of  $\alpha = 0$ , our results of  $S_{xx}$  and  $S_{xy}$  are in good agreement with theoretical results [67–69]

and experimental observations [64–66] of graphene except for the abnormal sign change around the zeroth LL of  $S_{xx}$ . For  $\alpha > 0$ , Seebeck coefficient  $S_{xx}$  and Nernst coefficient  $S_{xy}$  change strikingly and present a general trend as increasing the structure parameter  $\alpha$ . In the quantum limit, we explain the characteristics analytically. Moreover, our studies may motivate further experimental investigations on magnetothermoelectric properties of the  $\alpha - T_3$  model.

The remainder of this paper is organized as follows. In Sec. II, we show the tight-binding Hamiltonian. The Seebeck and Nernst coefficients are derived by combining the nonequilibrium Green's function and the Landauer-Büttiker formalism with the Stréda formula. In Sec. III, the numerical results of the Seebeck and Nernst coefficients are presented, including both the strong and weak magnetic field cases, and several interesting features in the numerical results are discussed analytically. Finally, conclusions are presented in Sec. IV.

## II. HAMILTONIAN AND FORMULA

We investigate four-terminal  $\alpha - T_3$  devices as shown in Figs. 1(c) and 1(d). In the presence of a perpendicular magnetic field, the tight-binding Hamiltonian considering only nearest-neighbor hopping is given by [52]

$$H = \sum_{(i,j)(j,k)} (t \cos \varphi e^{i\phi_{ij}} c_i^\dagger c_j + t \sin \varphi e^{i\phi_{jk}} c_j^\dagger c_k + \text{H.c.}) + \sum_{\gamma} w_{\gamma} c_{\gamma}^{\dagger} c_{\gamma}, \quad (1)$$

where  $\gamma = i, j, k$  are the coordinates of sublattices  $A$ ,  $B$ , and  $C$ , respectively.  $c_{i,j,k}^{\dagger}$  ( $c_{i,j,k}$ ) are creation (annihilation) operators at sublattices  $A$ ,  $B$ , and  $C$ . H.c. is the Hermitian conjugate. We consider on-site Anderson-type disorders only in the central scattering regions as denoted by the black dashed rectangles in Figs. 1(c) and 1(d). The on-site potential  $w_{\gamma}$  is assumed to distribute randomly between  $[-W/2, W/2]$ , with  $W$  as the strength of disorders. Due to the perpendicular uniform magnetic field  $B$ , an additional phase  $\phi_{ij(jk)} = (2\pi/\phi_0) \int_{i(j)}^{j(k)} \mathbf{A} \cdot d\mathbf{l}$  is added in the hopping term by the Peierls substitution with  $\phi_0 = h/e$  being the magnetic flux quantum, where the vector potential  $\mathbf{A}$  is described by  $(0, Bx, 0)$  in the lead-1,3 and central scattering region, and by  $(-By, 0, 0)$  in the lead-2,4. After the gauge transformation in the boundary, the magnetic flux per hexagon  $\Phi = BS_0 = \phi\phi_0$  with  $S_0$  the area of a hexagon and  $\phi$  the strength of the magnetic field. Here the Zeeman effect is neglected, so the spin is degenerate.

For the multiterminal  $\alpha - T_3$  device, the electric current and the heat current in lead- $n$  can be calculated from the Landauer-Büttiker formula [63,70–72]

$$I_n^C = \frac{-e}{h} \sum_m \int dE T_{nm}(E) [f_n(E) - f_m(E)],$$

$$I_n^Q = \frac{1}{h} \sum_m \int dE (E - E_F^n) T_{nm}(E) [f_n(E) - f_m(E)], \quad (2)$$

where  $f_n(E)$  is the Fermi-Dirac distribution function in lead- $n$  which can be written as

$$f_n(E, E_F^n, \mathcal{T}_n) = \frac{1}{e^{(E-E_F^n)/k_B(\mathcal{T}_n+\mathcal{T})} + 1},$$

$E_F^n = E_F - eV_n$  is the Fermi energy,  $V_n$  is the external voltage bias, and  $\mathcal{T}_n + \mathcal{T}$  is the temperature of lead- $n$ . Under low voltage bias and small temperature gradient, it can be expanded to the linear order in the Fermi energy and the temperature as

$$f_n(E) = f_0(E) + e \frac{\partial f_0}{\partial E} V_n + \frac{\partial f_0}{\partial \mathcal{T}} \mathcal{T}_n, \quad (3)$$

where  $f_0 = 1/[e^{(E-E_F)/k_B\mathcal{T}} + 1]$  is the Fermi-Dirac distribution under zero voltage bias and zero temperature bias. Therefore, in the linear response regime, the electric current  $\mathbf{I}_C = (I_1^C, I_2^C, I_3^C, I_4^C)^T$  and the heat current  $\mathbf{I}_Q = (I_1^Q, I_2^Q, I_3^Q, I_4^Q)^T$  can be expressed to linear order in  $\mathbf{V} = (V_1, V_2, V_3, V_4)^T$  and  $\mathcal{T}_n = (\mathcal{T}_1, \mathcal{T}_2, \mathcal{T}_3, \mathcal{T}_4)^T$  as the Stréda formula [63,70–72],

$$\begin{pmatrix} \mathbf{I}_C \\ \mathbf{I}_Q \end{pmatrix} = \begin{pmatrix} e^2 \mathbf{L}_0 & -e \mathbf{L}_1 \\ -e \mathbf{L}_1 & \mathbf{L}_2 \end{pmatrix} \begin{pmatrix} \mathbf{V} \\ \mathcal{T}_n/\mathcal{T} \end{pmatrix}, \quad (4)$$

where

$$L_{\eta, nm} = \frac{1}{h} \int dE (E - E_F)^\eta \left( -\frac{\partial f_0}{\partial E} \right) T_{nm}(E), \quad \eta = 0, 1, 2. \quad (5)$$

At low temperature, the electric contribution to the heat current dominates over the contribution of phonons, hence we neglect the effect of phonons here. Using the nonequilibrium Green's function method, we get the transmission coefficient  $T_{nm}(E) = \text{Tr}[\mathbf{\Gamma}_n \mathbf{G}^r \mathbf{\Gamma}_m \mathbf{G}^a]$  from lead- $m$  to lead- $n$  in Eqs. (2) and (5), where the linewidth functions  $\mathbf{\Gamma}_n(E) = i[\mathbf{\Sigma}_n^r(E) - \mathbf{\Sigma}_n^a(E)]$ . In addition, the retarded Green's function is  $\mathbf{G}^r(E) = [\mathbf{G}^a(E)]^\dagger = [\mathbf{E}\mathbf{I} - \mathbf{H}_C - \sum_n \mathbf{\Sigma}_n^r(E)]^{-1}$ , where  $\mathbf{H}_C$  is the Hamiltonian matrix in the central scattering region and  $\mathbf{I}$  is the identity matrix with the dimension equal to  $\mathbf{H}_C$ . The retarded self-energy function  $\mathbf{\Sigma}_n^r(E) = [\mathbf{\Sigma}_n^a(E)]^\dagger$  can be calculated by  $\mathbf{\Sigma}_n^r(E) = \mathbf{H}_{C,n} \mathbf{g}_n^r(E) \mathbf{H}_{n,C}$ , where  $\mathbf{H}_{C,n}$  ( $\mathbf{H}_{n,C}$ ) is the coupling from the central region (lead- $n$ ) to lead- $n$  (central region) and  $\mathbf{g}_n^r(E)$  is the surface retarded Green's function of the semi-infinite lead- $n$  which can be obtained by the recursive method [73–76].

The transport coefficients measured in experiments are under the condition  $\mathbf{I}_C = 0$  [70], so we have

$$\mathbf{V} = \mathbf{L}_0^{-1} \mathbf{L}_1 \mathcal{T}_n / e \mathcal{T}. \quad (6)$$

As shown in Figs. 1(c) and 1(d), a temperature gradient  $\Delta\mathcal{T}$  is applied between the longitudinal lead-1 and lead-3, i.e.,  $T_{1/3} = \mathcal{T} \pm \Delta\mathcal{T}/2$ . This longitudinal temperature gradient induces a longitudinal bias  $V_{1/3}$  and a transverse bias  $V_{2/4}$  by the Lorentz force under a perpendicular magnetic field. Then the Seebeck coefficient is defined as [77]

$$S_{xx} = - \lim_{\Delta\mathcal{T} \rightarrow 0} \frac{V_1 - V_3}{\Delta\mathcal{T}} \Big|_{\mathbf{I}_C=0} \quad (7)$$

and the Nernst coefficient is defined as [77]

$$S_{xy} = - \lim_{\Delta\mathcal{T} \rightarrow 0} \frac{V_2 - V_4}{\Delta\mathcal{T}} \Big|_{\mathbf{I}_C=0}. \quad (8)$$

### III. NUMERICAL RESULTS AND DISCUSSION

In this section, we present the numerical results of Seebeck coefficient  $S_{xx}$  and Nernst coefficient  $S_{xy}$  as functions of the Fermi energy  $E_F$  for different structure parameters  $\alpha$ . In the numerical calculations, the energy is measured in the unit of the hopping energy  $t$ . The widths of the zigzag  $\alpha - T_3$  nanoribbon  $3a_0n_z$  and that of armchair  $\alpha - T_3$  nanoribbon  $\sqrt{3}a_0n_a$  are described by integers  $n_z$  and  $n_a$ , respectively, with  $a_0$  being the bond length. In the schematic diagram of the four-terminal  $\alpha - T_3$  device of Fig. 1(c),  $n_z = 2$  and  $n_a = 5$ . In Fig. 1(d),  $n_a = 3$  and  $n_z = 3$ . The zigzag and armchair four-terminal  $\alpha - T_3$  devices are defined by the edge patterns along the  $x$  direction, i.e., by the lead-1,3 and the central region. Therefore, the four-terminal  $\alpha - T_3$  devices in Figs. 1(c) and 1(d) are zigzag and armchair, respectively.

#### A. The influence of the structure parameter $\alpha$

First, we study the influence of the structure parameter  $\alpha$  on the Seebeck and Nernst coefficients in the vicinity of the Dirac point under a strong magnetic field. In this case, LLs form. Seebeck and Nernst coefficients are independent of the edge pattern of the nanoribbon, as will be proved later in this section. Hence, there's no harm to choose the four-terminal zigzag device as shown in Fig. 1(c) to study the Seebeck and Nernst effects. Figure 2 shows the Seebeck coefficient  $S_{xx}$  and Nernst coefficient  $S_{xy}$  as functions of  $E_F$  at different temperatures  $k_B\mathcal{T} = 0.003t$ ,  $0.005t$ , and  $0.007t$  for different structure parameters  $\alpha$ . For clarity, in Figs. 2(a1)–2(a4), the energy bands are shown as background by the dashed gray line. Generally, we can see in Fig. 2 that  $S_{xx}$  is odd, i.e.,  $S_{xx}(E_F) = -S_{xx}(-E_F)$  and  $S_{xy}$  is even, i.e.,  $S_{xy}(E_F) = -S_{xy}(E_F)$ . Therefore, unless otherwise specifically stated, we mainly focus on the regime of  $E_F \leq 0$  in the following.

For  $\alpha = 0$ , the Nernst coefficient  $S_{xy}(E_F)$  shows peaks near  $E_F = 0$  as displayed in Fig. 2(c1). Meanwhile, as shown in Fig. 2(a1), our results of  $S_{xx}$  are in good agreement with other theoretical results [67–69] and experimental observations [64–66] of graphene for both holes and electrons. That is,  $S_{xx}$  shows positive (negative) peaks as Fermi energy  $E_F$  crossing the LLs on the hole (electron) side. However, our results of the zeroth LL, consistent with other theoretical results [67–69], are different from the experimental observation [64–66]. Similarly, with the higher LLs as shown in Fig. 2(a1), the theoretical results of  $S_{xx}$  show positive (negative) peak as Fermi energy  $E_F < (>)0$  and decrease when  $E_F$  passes the Dirac point increasingly [67–69]. On the contrary, in the experimental observation,  $S_{xx}$  shows a negative (positive) peak as Fermi energy  $E_F < (>)0$  and increases when  $E_F$  passes the Dirac point [64–66]. This pair of  $S_{xx}$  peaks near the zeroth LL shows an opposite sign between the theoretical results [67–69] and experimental observations [64–66].

Increasing  $\alpha$  from zero, the Berry phase changes continuously [12] and the valley-pseudospin degeneracies of LLs are removed, which are shown clearly in the spectra by dashed gray lines in Figs. 2(a2)–2(a4). When  $\alpha = 1$ , the LLs of two valley pseudospins are doubly degenerated again. Therefore, as shown in Figs. 2(a2)–2(a4), when  $\alpha$  increases from zero, the peaks of the Seebeck coefficient  $S_{xx}$  split into two due to



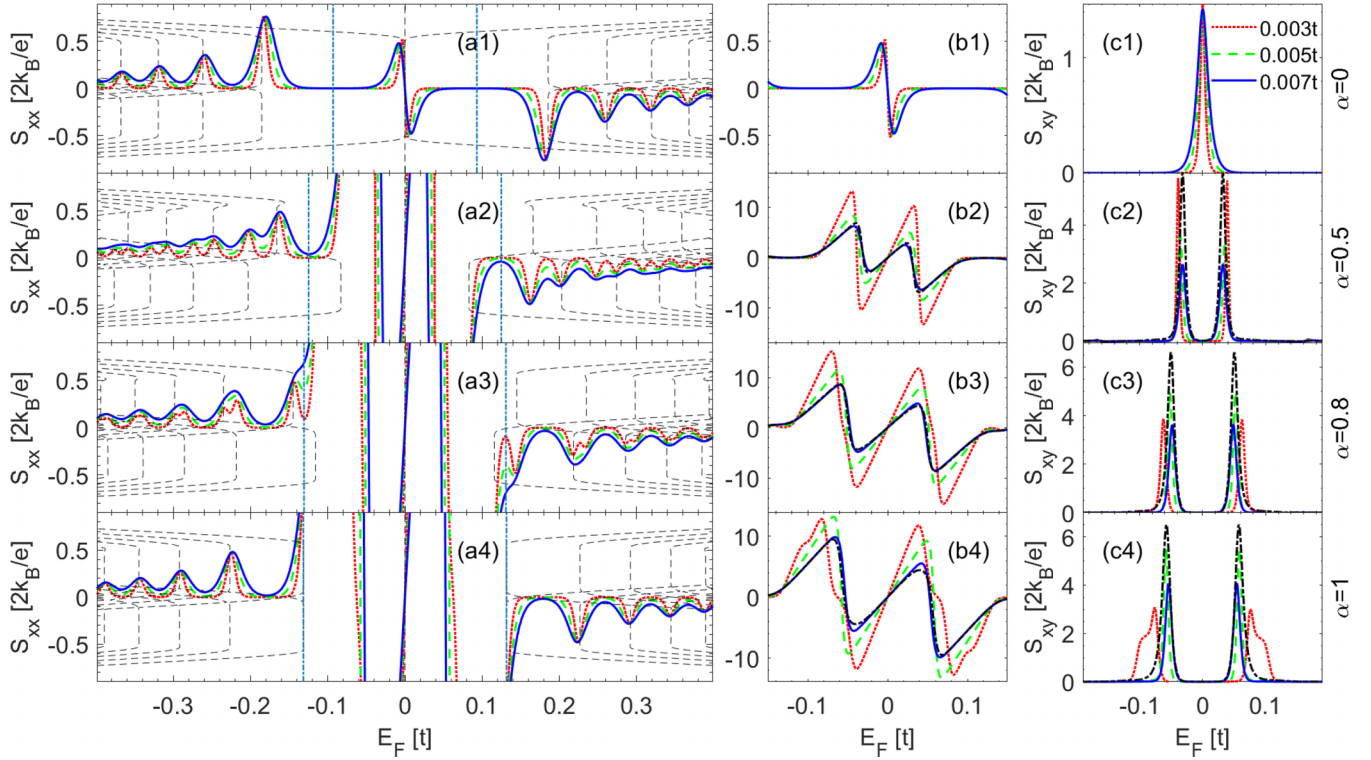


FIG. 2. (a1)–(a4) Seebeck coefficient  $S_{xx}$ , energy bands (dashed gray lines), and  $\pm E_c$  (dash-dotted light blue lines). (c1)–(c4) Nernst coefficient  $S_{xy}$  as functions of  $E_F$  for  $\alpha = 0, 0.5, 0.8, 1$ , which is noted on the right of each column in the four-terminal zigzag device [see Fig. 1(c)]. Different curves are for different temperatures  $k_B T = 0.003t, 0.005t$ , and  $0.007t$ , respectively, as shown in the legend. (b1)–(b4) Zoom-in of panels (a1)–(a4), respectively. The dash-dotted black lines in (b1)–(b4) and (c1)–(c4) are plotted by analytical results at  $k_B T = 0.007t$ . Other parameters are  $\phi = 0.01, W = 0$ , and  $n_z = n_a = 60$ .

the valley-pseudospin degeneracy being removed. The series of peaks of one valley pseudospin shifts right and the series of peaks of the other valley pseudospin moves to left. When  $\alpha = 1$ , two adjacent peaks combine into a single peak again. That is, similar to  $\alpha = 0$ , when  $\alpha > 0$  the Seebeck coefficient  $S_{xx}$  displays a series of positive (negative) peaks as Fermi energy  $E_F < (>) 0$  at the LLs as shown in Figs. 2(a2)–2(a4). On the other hand, the peak of  $S_{xy}$  for  $\alpha = 0$  splits into double peaks near the lowest LLs for  $\alpha > 0$  and the height is enhanced.

Interestingly, there exhibit three distinctive features for  $\alpha > 0$  which are not present in the case of  $\alpha = 0$ . First, we investigate the regime of  $|E_F| > E_c$  with  $E_c = (1 + \alpha)E_0/\sqrt{2(1 + \alpha^2)}$ , where  $E_0 = \sqrt{2\sqrt{3}\phi t}$ .  $\pm E_c$  are plotted by dash-dotted light blue lines in Figs. 2(a1)–2(a4). Figure 3 shows the inverse of the peak height of Seebeck coefficient  $S_{xx}$  ( $1/S_{xx}^{\text{peak}}$ ) as a function of the peak number  $n_p$  with the different structure parameters  $\alpha = 0, 0.5$ , and  $1$ , respectively. The data points are obtained from the curves of  $k_B T = 0.003t$  in Figs. 2(a1)–2(a4). Here the peak number  $n_p$  denotes the  $n_p$ th peak near the Dirac point in the regime of  $|E_F| > E_c$ . We can see that for  $\alpha = 1$  the inverse of the peak height of  $S_{xx}$  is  $\frac{-e}{\ln 2k_B} [n_p + \text{sign}(n_p)\delta]$  with  $\delta = 1/2$  and  $\text{sign}(n_p) = 1$  for  $n_p > 0$  and  $-1$  for  $n_p < 0$ . This is similar to that in the conventional metal [70]. On the other hand, for  $\alpha = 0$  the inverse of the peak height of  $S_{xx}$  is  $\frac{-e}{\ln 2k_B} [n_p + \text{sign}(n_p)\delta]$  with  $\delta = 0$ , which is in a good agreement with the result of graphene in Refs. [63,64]. It was considered that the pseudospin-related

Berry phase introduced the additional phase shift which induced  $\delta$  from  $1/2$  in the conventional metal to  $0$  in graphene [63,64]. As is well-known that a characteristic feature of the  $\alpha - T_3$  model is that the Berry phase changes continuously from  $\pi$  to  $0$  as increasing  $\alpha$  from  $0$  to  $1$ , it is natural to ask how  $\delta$  changes for intermediate value  $\alpha$  between  $0$  and  $1$ . Interestingly, Fig. 3 shows that for  $\alpha = 0.5$  the inverse of

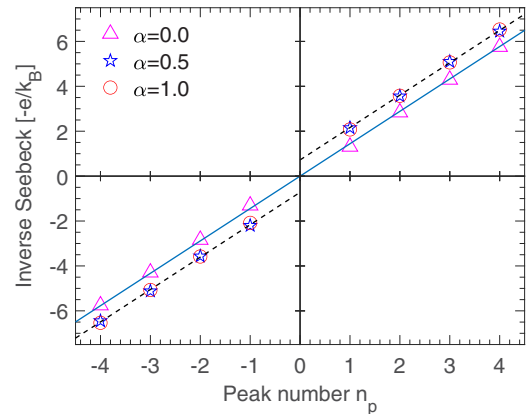


FIG. 3. The inverse of peak height of the Seebeck coefficients  $S_{xx}$  as a function of the peak number  $n_p$ . These data points are obtained from the curves of  $k_B T = 0.003t$  in Fig. 2. The blue line is  $\frac{-e}{k_B} n_p / \ln 2$  and the dashed black lines are  $\frac{-e}{k_B} [n_p + \text{sign}(n_p)/2] / \ln 2$ .

the peak height of  $S_{xx}$  is  $\frac{-e}{\ln 2k_B} [n_p + \text{sign}(n_p)\delta]$  with  $\delta = 1/2$ , which is the same with  $\alpha = 1$  and independent of the variable Berry phase.

Second, for lower Fermi energy, i.e.,  $E_c \gtrsim |E_F| \gg 0$ , we can see the highest positive (negative) peak of  $S_{xx}$  as Fermi energy  $E_F < (>)0$  in Figs. 2(b2)–2(b4), which is much higher than other peaks in Figs. 2(a2)–2(a4). The enhancement of the highest positive (negative) peak can be understood as being due to the appearance of the bulk energy gap between the flat band and lowest LL when  $\alpha > 0$ . In other words, a large bias is needed to balance the thermal forces on the charge carriers in the bulk energy gap, therefore high  $S_{xx}$  is induced.

Finally, when close to the Dirac point, i.e.,  $|E_F| \sim 0$ , the sign of the peak near the flat band is opposite that of the higher LLs peaks. That is,  $S_{xx}$  displays a negative (positive) peak as Fermi energy  $E_F < (>)0$  near the flat band. As will be illustrated analytically in the following, this opposite sign of peaks of  $S_{xx}$  near the Dirac point is mainly due to the isolated flat band, which was also noted by Ref. [62] in the absence of magnetic field.

In the following subsection, we will present analytical discussions to explain these unique features in the  $\alpha - T_3$  model for  $\alpha > 0$ .

### B. Analytic discussion

To further investigate the characteristic signatures of the  $\alpha - T_3$  model for  $\alpha > 0$ , we calculate Seebeck and Nernst coefficients analytically by the low-energy effective Hamiltonian in the clean limit under strong magnetic field. In this limit case, the distance between LLs is greater than the temperature broadening, which is greater than the impurity broadening. We consider a simple case in which the impurity scattering rate  $\Gamma$  is constant. In the linear response regime, Seebeck and Nernst coefficients can be given by the Kube-Stréda formula [67]

$$\mathbf{S} = \hat{\sigma}^{-1} \hat{\alpha} = \begin{pmatrix} \frac{\sigma_{xx}\alpha_{xx} + \sigma_{xy}\alpha_{xy}}{\sigma_{xx}^2 + \sigma_{xy}^2} & \frac{\sigma_{xx}\alpha_{xy} - \sigma_{xy}\alpha_{xx}}{\sigma_{xx}^2 + \sigma_{xy}^2} \\ \frac{\sigma_{xy}\alpha_{xx} - \sigma_{xx}\alpha_{xy}}{\sigma_{xx}^2 + \sigma_{xy}^2} & \frac{\sigma_{xx}\alpha_{xx} + \sigma_{xy}\alpha_{xy}}{\sigma_{xx}^2 + \sigma_{xy}^2} \end{pmatrix}, \quad (9)$$

where  $\hat{\sigma}$  is the electrical conductivity tensor and  $\sigma_{ji}(E_F, T) = \int d\epsilon \sigma_{ji}(\epsilon) (-\frac{\partial f_0(\epsilon)}{\partial \epsilon})$ ,  $\hat{\alpha}$  is the thermoelectric conductivity tensor, and  $\alpha_{ji}(E_F, T) = \frac{-1}{eT} \int d\epsilon \sigma_{ji}(\epsilon) (\epsilon - E_F) (-\frac{\partial f_0(\epsilon)}{\partial \epsilon})$ . Considering the energy  $\epsilon \rightarrow 0$ , the longitudinal conductivity is

$$\sigma_{xx}(\epsilon) = C_F^A \frac{\Gamma^2}{\epsilon^2 + \Gamma^2}. \quad (10)$$

$C_F^A$  is a constant and details about our calculations can be found in the Appendixes. In the clean limit and  $T = 0$ , the Hall conductivity in our systems is [24]

$$\sigma_{xy}(\epsilon) = \frac{-\text{sign}(\epsilon)2e^2}{h} \left( \left[ \frac{\epsilon^2}{E_0^2} + \frac{1}{1 + \alpha^2} \right] + \left[ \frac{\epsilon^2}{E_0^2} + \frac{\alpha^2}{1 + \alpha^2} \right] \right). \quad (11)$$

Here,  $[x]$  is the integer part of  $x$ , which counts levels crossed by  $\epsilon$ . In the limiting case  $\alpha = 0$ , the Hall plateaus are 1,3,5,7,... in units of  $-2e^2/h$ , which are the same with relativistic graphene. In the other limiting case  $\alpha = 1$ , the Hall

series is 0,2,4,6,..., again in units of  $-2e^2/h$ . Intermediately, for  $0 < \alpha < 1$ , the Hall series in units of  $-2e^2/h$  is 0,1,2,3,...

In the regime of  $|E_F| > E_c$ , because the conductivity  $\sigma_{xy}$  plateaus and  $\sigma_{xx}$  vanishes, the contribution of  $\sigma_{xy}$  and  $\alpha_{xy}$  to thermoelectric power is dominated. The Seebeck coefficient in Eq. (9) is simplified to  $S_{xx} = \alpha_{xy}/\sigma_{xy}$  and the Nernst coefficient vanishes. When the Fermi energy is located at a LL, we have  $\sigma_{xy}(\epsilon) = \sigma_{xy}^<$  for  $\epsilon < E_F$  and  $\sigma_{xy}(\epsilon) = \sigma_{xy}^>$  for  $\epsilon > E_F$ , where  $\sigma_{xy}^<(>)$  are constants and could be obtained in Eq. (11).

Thus, the peak value of  $S_{xx} = \frac{-2 \ln 2k_B}{e} \frac{\sigma_{xy}^> - \sigma_{xy}^<}{\sigma_{xy}^> + \sigma_{xy}^<}$  is obtained by analytical calculations.  $\sigma_{xy}$ , the inverse of the  $n_p$ th peak height of  $S_{xx}$ , and the peak number  $n_p$  are shown in Table I. The function relation between the inverse of the peak height of  $S_{xx}$  and the peak number  $n_p$ , i.e.,  $\frac{1}{S_{xx}^{\text{peak}}} = \frac{-e}{\ln 2k_B} [n_p + \text{sign}(n_p)\delta]$  with  $\delta = 0$  for  $\alpha = 0$  and  $\delta = 1/2$  for  $\alpha > 0$ , could be obtained again analytically. Therefore,  $\delta$  is dominated by the Hall plateau series. As long as the temperature is low enough to remove the valley-pseudospin degeneracy,  $\delta$  is 1/2 for intermediate value  $\alpha$  between 0 and 1 as shown for  $\alpha = 0.5$  in Fig. 3. However, because of the influence of temperatures [see Fig. 2(a3) for  $\alpha = 0.8$ ], some peaks of  $S_{xx}$  may be valley-pseudospin double degeneracy and some are not degenerated. Both the peak height and peak number may be irregular. Hence, the inverse of the peak height of Seebeck coefficient  $S_{xx}$  would not satisfy the relation of  $\frac{-e}{\ln 2k_B} [n_p + \text{sign}(n_p)\delta]$ . We hope our results could help to motivate further experimental observations and clear up unnecessary controversies.

In the limit regime  $|E_F| \sim 0$ , because of the particular LLs for  $\alpha > 0$  in  $\alpha - T_3$  model, we have  $\sigma_{xy}(E_F, T) = 0$  and  $\alpha_{xy}(E_F, T) = 0$ . Therefore, the Seebeck coefficient in Eq. (9) is simplified to  $S_{xx} = \alpha_{xx}/\sigma_{xx}$  and the Nernst coefficient vanishes. On the other hand, due to the flat band for  $\alpha > 0$  in the  $\alpha - T_3$  model, considering the energy  $\epsilon \rightarrow 0$ , the longitudinal conductivity is (details of calculation is in Appendix C)

$$\sigma_{xx}(\epsilon) = C_F^A \frac{\Gamma^2}{\epsilon^2 + \Gamma^2}. \quad (12)$$

As shown schematically by the dashed orange lines in Figs. 4(a)–4(c), the negative (positive) peak of  $S_{xx}$  as Fermi energy  $E_F < (>)0$  is due to the negative (positive) peak of  $\alpha_{xx}$ . Comparing with the solid light blue line which is calculated by Eq. (9) confirms that  $\alpha_{xx}/\sigma_{xx}$  dominates in this limit regime. Therefore, we find that the negative (positive) peak of  $S_{xx}$  as Fermi energy  $E_F < (>)0$  is induced by both the nonzero longitudinal conductivity because of the flat band and  $\sigma_{xy}(E_F, T) = 0$  for  $E_F$  near the Dirac point.

In regime  $0 \ll |E_F| \lesssim E_c$ , due to the thermal broadening,  $\sigma_{xy}(E_F, T)$  vanishes faster than  $\alpha_{xy}(E_F, T)$  for  $\alpha = 0.5$  at  $k_B T = 0.007t$  and  $\phi = 0.01$  as shown by the dotted yellow lines in Figs. 4(c)–4(e). This is the key point which induces the huge positive peak of  $S_{xx}$ . As shown in Fig. 4(c), the good agreement between the dotted yellow line and the solid light blue line implies that  $\alpha_{xy}/\sigma_{xy}$  dominates in this regime. In the mediate regime, Eq. (9) is necessary due to both approximations  $\alpha_{xx}/\sigma_{xx}$  and  $\alpha_{xy}/\sigma_{xy}$  failing. The analytical results by Eq. (9) are shown by the dash-dotted black lines in Figs. 3(b1)–3(b4) and 3(c1)–3(c4) at  $k_B T =$

TABLE I. The inverse of peak height of  $S_{xx}$  for  $\alpha = 0, 0.5, 1$  in the regime of  $E_F > E_c$ , where  $E_c = (1 + \alpha)E_0/\sqrt{2(1 + \alpha^2)}$  and  $E_0 = \sqrt{2\sqrt{3}\phi t}$ .

$\alpha = 0$	$\sigma_{xy}[-2e^2/h]$	1	3	5	7	...	$\frac{1}{S_{xx}^{\text{peak}}} = \frac{-en_p}{\ln 2k_B}$
	$1/S_{xx}^{\text{peak}}[\frac{-e}{2\ln 2k_B}]$	2	4	6	8	...	
	peak number $n_p$	1	2	3	...	...	
$\alpha = 1$	$\sigma_{xy}[-2e^2/h]$	2	4	6	8	...	$\frac{1}{S_{xx}^{\text{peak}}} = \frac{-e(n_p+1/2)}{\ln 2k_B}$
	$1/S_{xx}^{\text{peak}}[\frac{-e}{2\ln 2k_B}]$	3	5	7	...	...	
	peak number $n_p$	1	2	3	...	...	
$\alpha = 0.5$	$\sigma_{xy}[-2e^2/h]$	1	2	3	4	...	$\frac{1}{S_{xx}^{\text{peak}}} = \frac{-e(n_p+1/2)}{\ln 2k_B}$
	$1/S_{xx}^{\text{peak}}[\frac{-e}{2\ln 2k_B}]$	3	5	7	...	...	
	peak number $n_p$	1	2	3	...	...	

$0.007t$ . For  $S_{xx}$ , the numerical results and analytical results have good agreement. For  $S_{xy}$ , the results are consistent qualitatively.

### C. Effects of temperatures and disorders

Next, we explore the effect of temperatures. With the increase of temperature, the amplitude of the highest positive peak and the negative peak of  $S_{xx}$  with  $\alpha > 0$  decreases as shown in Figs. 2(b2)–2(b4). Nevertheless, the other peaks

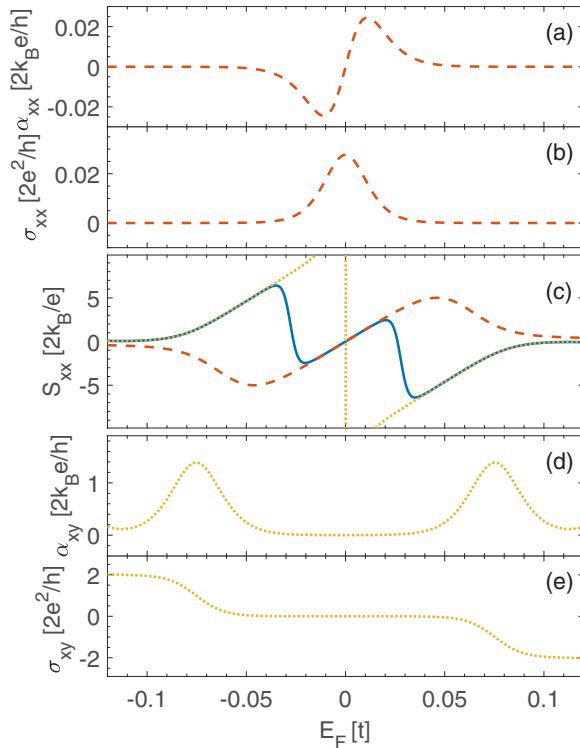


FIG. 4. Analytical results in clean limit for  $\alpha = 0.5$  at  $k_B T = 0.007t$  and  $\phi = 0.01$ . (a)  $\alpha_{xx}$ , (b)  $\sigma_{xx}$ , (c)  $S_{xx}$ , (d)  $\alpha_{xy}$ , and (e)  $\sigma_{xy}$ . The dashed orange line in (c) is calculated by  $\alpha_{xx}/\sigma_{xx}$ . The dotted yellow line in (c) is calculated by  $\alpha_{xy}/\sigma_{xy}$ . The solid light blue line is calculated by  $(\sigma_{xx}\alpha_{xx} + \sigma_{xy}\alpha_{xy})/(\sigma_{xx}^2 + \sigma_{xy}^2)$ .

only broaden and roughly remain unchanged in height, so the valleys between the adjacent peaks rise in the regime of  $E_F < 0$ . By increasing the temperature  $k_B T$  to exceed the nearest LL spacing, the nearest peaks of  $S_{xx}$  overlap with each other and finally merge together to form a larger peak as shown in Fig. 2(a3). Meanwhile, in the case of  $\alpha = 0$ , the temperature effect on Nernst coefficient  $S_{xy}$  shown in Fig. 2(c1) is similar to  $S_{xx}$ . In the case of  $\alpha > 0$ , Figs. 2(c2)–2(c4) show that the positions of the double peaks of  $S_{xy}$  shift towards the Dirac point.

In addition, let us investigate the effect of disorders. Figure 5 shows the Seebeck coefficient  $S_{xx}$  and Nernst coefficient  $S_{xy}$  as functions of  $E_F$  for  $\alpha = 0, 0.5, 1$  with disorder strength  $W = 0.1t, 0.3t, 0.5t, 0.8t$  in the four-terminal zigzag device under strong magnetic field  $\phi = 0.01$ . The results are calculated by averaging up to 500 random disorder configurations. For  $\alpha = 0$ , we can see from Fig. 5(a1) that the Seebeck coefficient  $S_{xx}$  is robust to disorders because of the existence of LLs, except that the peak height is slightly decreased near the Dirac point. On the other hand, as shown in Fig. 5(b1), disorders

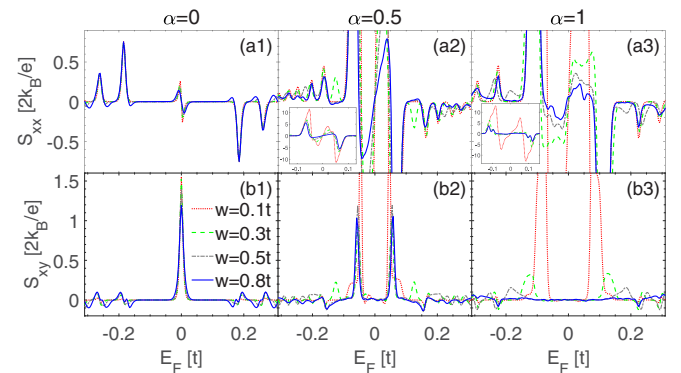


FIG. 5. (a1)–(a3) Seebeck coefficient  $S_{xx}$  and (b1)–(b3) Nernst coefficient  $S_{xy}$  as functions of  $E_F$  for  $\alpha = 0, 0.5, 1$  with disorder strength  $W = 0.1t, 0.3t, 0.5t, 0.8t$  in the four-terminal zigzag device [see Fig. 1(c)]. The insets in (a2) and (a3) are the zoom-in of (a2) and (a3). The results are averaged over up to 500 random disorder configurations. Other parameters are  $\phi = 0.01$ ,  $k_B T = 0.003t$ , and  $n_z = n_a = 40$ .

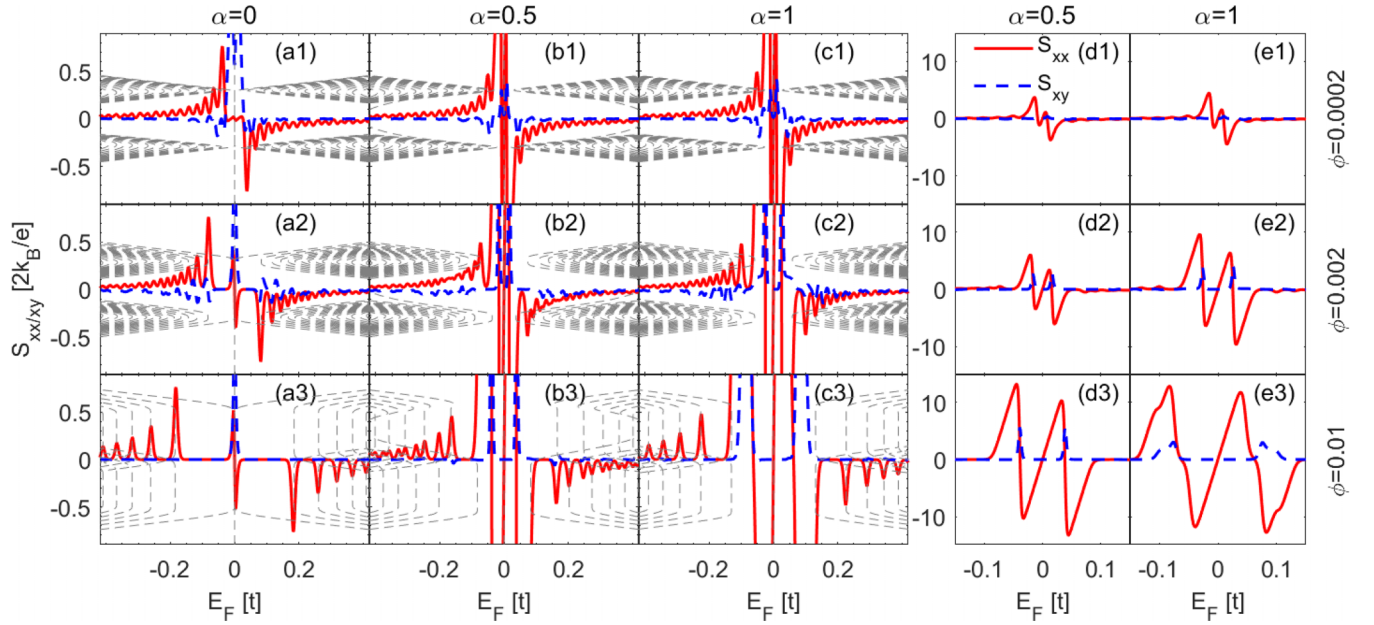


FIG. 6. Seebeck coefficient  $S_{xx}$  and Nernst coefficient  $S_{xy}$  as functions of  $E_F$  for (a1)–(a3)  $\alpha = 0$ , (b1)–(b3)  $\alpha = 0.5$ , and (c1)–(c3)  $\alpha = 1$  under different magnetic fields  $\phi = 0.0002, 0.002, 0.01$  in the four-terminal zigzag device [see Fig. 1(c)]. The dashed gray lines are energy bands. (d1–d3) and (e1)–(e3) are the zoom-in of (b1)–(b3) and (c1)–(c3), respectively. Other parameters are  $k_B T = 0.003t$ ,  $W = 0$ , and  $n_z = n_a = 60$ .

induce oscillations of the Nernst coefficient  $S_{xy}$  at each LL energy except that the peak height is slightly decreased near the Dirac point. This result of  $S_{xy}$  is in good agreement with the theoretical results [67–69] and experimental observations [64–66] of the Nernst coefficient in graphene. For  $\alpha > 0$ , the peak height of  $S_{xx}$  and the oscillation amplitude of  $S_{xy}$  are decreased by increasing the strength of the disorder [see Figs. 5(a2)–5(a3), 5(b2), and 5(b3)]. Especially, the highest positive peak of  $S_{xx}$  and the double peaks near the Dirac point of  $S_{xy}$  are suppressed obviously [see the insets of Figs. 5(a2), 5(a3), 5(b2), and 5(b3)]. It reveals that the bigger value  $\alpha$  is, the less robust the Seebeck and Nernst effect are.

#### D. Effects of the magnetic field strength $\phi$ and edge patterns

Finally, we examine the influence of the magnetic field strength  $\phi$  and edge patterns on the Seebeck coefficient  $S_{xx}$  and Nernst coefficient  $S_{xy}$ . In Figs. 6 and 7, we plot  $S_{xx}$  and  $S_{xy}$  as functions of  $E_F$  under different magnetic fields for different structure parameters  $\alpha$  in zigzag and armchair devices, respectively. For clarity, the energy bands are shown as background by dashed gray lines for each  $\alpha$  and  $\phi$ . In the weak magnetic field, because of the different band structures for the zigzag and armchair nanoribbons, the Seebeck coefficient  $S_{xx}$  and Nernst coefficient  $S_{xy}$  strongly depend on the edge patterns. When  $E_F < 0$ , the positive peaks of  $S_{xx}$  are irregular for the armchair device while are still regularly distributed for the zigzag device. On the other hand,  $S_{xy}$  oscillates around zero differently for both the zigzag and armchair devices near the Dirac point. When  $E_F$  is far from the Dirac point, both  $S_{xx}$  and  $S_{xy}$  tend to zero. By increasing the magnetic field, the LLs are gradually formed from the Dirac point to the high  $E_F$ . As shown in the spectra of Figs. 6(a3), 6(b3), 6(c3), 7(a3), 7(b3), and 7(c3) under the high magnetic field  $\phi = 0.01$ ,

the LLs are completely formed for  $|E_F| < 0.4$ . The Seebeck and Nernst coefficients for zigzag and armchair devices are independent of the edge patterns, although the spectra at the edges dependent on the edge patterns. As shown in panels (d1)–(d3) and (e1)–(e3) in both Figs. 6 and 7, the highest positive peak and the negative peak near the Dirac point of  $S_{xx}$  because of the isolated flat band and the bulk energy gap regardless of the edge pattern of the device. The amplitude of the highest positive peak and negative peak of  $S_{xx}$  increases when the magnetic field increases from weak to strong due to the increasing of the band gap.

#### IV. CONCLUSION

In conclusion, by combining the nonequilibrium Green's function and the Landauer-Büttiker formalism with the Stréda formula, Seebeck and Nernst effects of pseudospin-1 fermions in four-terminal  $\alpha - T_3$  devices under magnetic fields are investigated numerically. It is shown that the Seebeck coefficient  $S_{xx}$  is an odd function and Nernst coefficient is an even function of the Fermi energy  $E_F$ . Under strong magnetic field,  $S_{xx}$  shows peaks when  $E_F$  crosses the LLs and the peak of  $S_{xy}$  for  $\alpha = 0$  splits into double peaks near the lowest LLs for  $\alpha > 0$  as expected. What's more, there show several characteristic features of  $S_{xx}$  for  $\alpha > 0$ . We discuss in detail these interesting features analytically and their relations with the corresponding band structures. In the regime  $|E_F| > E_c$ , we find that the inverse of the peak height of  $S_{xx}$  is  $\frac{-e}{\ln 2k_B} [n_p + \text{sign}(n_p)\delta]$ , with  $\delta = 0$  for  $\alpha = 0$  and  $\delta = 1/2$  for  $\alpha > 0$ . We show that  $\delta$  is determined by the Hall plateau series. Then, in the regime  $0 \ll |E_F| \lesssim E_c$ , there shows the highest positive peak of  $S_{xx}$  in Figs. 2(b2)–2(b4), which is much higher than other peaks in Figs. 2(a2)–2(a4). This highest positive peak



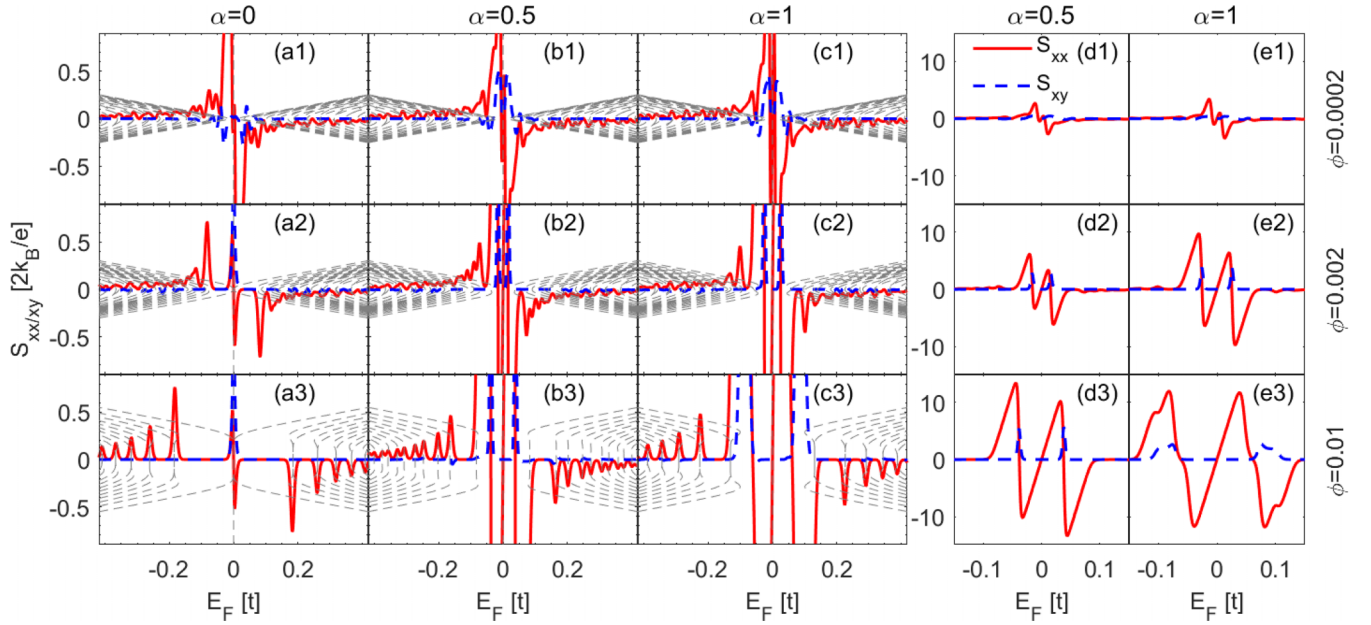


FIG. 7. Seebeck coefficient  $S_{xx}$  and Nernst coefficient  $S_{xy}$  as functions of  $E_F$  for (a1)–(a3)  $\alpha = 0$ , (b1)–(b3)  $\alpha = 0.5$ , (c1)–(c3)  $\alpha = 1$  under different magnetic fields  $\phi = 0.0002, 0.002, 0.01$  in the four-terminal armchair device [see in Fig. 1(d)]. The dashed gray lines are energy bands. (d1–d3) and (e1)–(e3) are the zoom-in of (b1)–(b3) and (c1)–(c3), respectively. Other parameters are  $k_B T = 0.003t$ ,  $W = 0$ , and  $n_z = n_a = 60$ .

is ascribed to the vanishing of the Hall conductivity due to the energy gap between the flat band and lowest LL. In addition, in the limit regime  $|E_F| \sim 0$ , there represents a negative peak in Figs. 2(a2)–2(a4). We relate this unique behavior to the vanishing of the Hall conductivity and the isolated flat band.

By increasing temperature, the amplitude of the highest positive peak and negative peak of  $S_{xx}$  with  $\alpha > 0$  decreases. Nevertheless, the other peaks only broaden and roughly remain unchanged in height. When the temperature  $k_B T$  exceeds the nearest LL spacing, the nearest peaks of  $S_{xx}$  overlap with each other and finally merge together to form a larger peak. Moreover, we also investigate the effect of disorders under strong magnetic field. Disorders induce oscillations of the Nernst coefficient  $S_{xy}$  at higher LL energy. It is found that by increasing  $\alpha$ , the system is more sensitive to disorders. Apart from the abnormal Seebeck coefficient near  $E_F = 0$ , our results for  $\alpha = 0$  are in good agreement with the theoretical results [67–69] and experimental observations [64–66] in graphene.

Finally, we show that the Seebeck coefficient  $S_{xx}$  and Nernst coefficient  $S_{xy}$  are strongly dependent on the edge patterns under weak magnetic fields. When the magnetic field increases from weak to strong, the results of  $S_{xx}$  and  $S_{xy}$  in zigzag device and armchair devices tend to the same. We hope these findings would provide a theoretical foundation for future experimental studies on the thermoelectric properties of materials based on the  $\alpha - T_3$  model.

#### ACKNOWLEDGMENTS

We thank S. A. Yang, Y. Xue, and Y. Wang for helpful discussions. We gratefully acknowledge the financial support from the National Natural Science Foundation of China (NSFC Grant No. 12004111).

#### APPENDIX A: LANDAU LEVELS AND WAVE FUNCTIONS OF $\alpha - T_3$ MODEL UNDER STRONG MAGNETIC FIELD

The low-energy effective Hamiltonian of  $\alpha - T_3$  under uniform magnetic field  $B = (0, 0, B)$  is [12]

$$H = v_F \begin{pmatrix} 0 & (s\pi_x - i\pi_y) \cos(\varphi) & 0 \\ (s\pi_x + i\pi_y) \cos(\varphi) & 0 & (s\pi_x - i\pi_y) \sin(\varphi) \\ 0 & (s\pi_x + i\pi_y) \sin(\varphi) & 0 \end{pmatrix}, \quad (\text{A1})$$

where  $\boldsymbol{\pi} = \mathbf{p} + e\mathbf{A}$ , with  $\mathbf{p}$  being the electron momentum operator and  $\mathbf{A}$  the vector potential given by  $\mathbf{A} = (0, Bx, 0)$  in the Landau gauge. In general,  $[\pi_i, \pi_j] = -ie^{ijk} \hbar e B_k$  with  $i, j, k = (x, y, z)$ . In this case, we have  $[\pi_x, \pi_y] = -i\hbar e B$ . For

convenience, we define the magnetic length  $l_B = \sqrt{\frac{\hbar}{|eB|}}$  and energy unit  $E_0 = \frac{\sqrt{2}\hbar v_F}{l_B} = \sqrt{2\sqrt{3}}\phi t$ . Then the raising and lowering ladder operators for the K valley are defined by



$a = \frac{l_B}{\sqrt{2}\hbar}(\pi_x - i\pi_y)$  and  $a^\dagger = \frac{l_B}{\sqrt{2}\hbar}(\pi_x + i\pi_y)$ , with  $[a, a^\dagger] = 1$ . Their actions on the Fock states  $|n\rangle$  are  $a|n\rangle = \sqrt{n}|n-1\rangle$  and  $a^\dagger|n\rangle = \sqrt{n+1}|n+1\rangle$ . The Hamiltonian of the K valley could be written as

$$H = E_0 \begin{pmatrix} 0 & a \cos(\varphi) & 0 \\ a^\dagger \cos(\varphi) & 0 & a \sin(\varphi) \\ 0 & a^\dagger \sin(\varphi) & 0 \end{pmatrix}. \quad (\text{A2})$$

Similarly, the Hamiltonian of the K' valley is obtained through the substitution  $a \rightarrow -a^\dagger$ . In summary, the eigenvalues are

$$E(n, \lambda, s, k_y) = \lambda \sqrt{n + \chi_s} E_0, \quad (\text{A3})$$

where  $n \geq 0$  is the integer,  $\lambda = \pm$  denotes the conductance and valence band,  $s = \pm$  represents the K/K' valley,  $k_y$  is the good quantum number along y axis,  $\chi_+ = \sin^2(\varphi)$ , and  $\chi_- = \cos^2(\varphi)$ . The corresponding wave functions are

$$|n, \lambda, s = +, k_y\rangle = \frac{e^{ik_y y}}{\sqrt{L_y}} \frac{1}{\sqrt{2}} \begin{pmatrix} \frac{\sqrt{n(1-\chi_+)}}{\sqrt{n+\chi_+}} |n-1\rangle \\ \lambda |n\rangle \\ \frac{\sqrt{(n+1)\chi_+}}{\sqrt{n+\chi_+}} |n+1\rangle \end{pmatrix} \quad (\text{A4})$$

and

$$|n, \lambda, s = -, k_y\rangle = \frac{e^{ik_y y}}{\sqrt{L_y}} \frac{1}{\sqrt{2}} \begin{pmatrix} \frac{\sqrt{(n+1)\chi_-}}{\sqrt{n+\chi_-}} |n+1\rangle \\ -\lambda |n\rangle \\ \frac{\sqrt{n(1-\chi_-)}}{\sqrt{n+\chi_-}} |n-1\rangle \end{pmatrix}. \quad (\text{A5})$$

For the flat band, the eigenvalues are

$$E(n, F, s, k_y) = 0. \quad (\text{A6})$$

The corresponding wave functions are

$$|n > 0, F, s = +, k_y\rangle = \frac{e^{ik_y y}}{\sqrt{L_y}} \begin{pmatrix} \frac{\sqrt{(n+1)\chi_+}}{\sqrt{n+\chi_+}} |n-1\rangle \\ 0 \\ -\frac{\sqrt{n(1-\chi_+)}}{\sqrt{n+\chi_+}} |n+1\rangle \end{pmatrix}, \quad (\text{A7})$$

$$|n = 0, F, s = +, k_y\rangle = \frac{e^{ik_y y}}{\sqrt{L_y}} \begin{pmatrix} 0 \\ 0 \\ |0\rangle \end{pmatrix}, \quad (\text{A8})$$

$$|n > 0, F, s = -, k_y\rangle = \frac{e^{ik_y y}}{\sqrt{L_y}} \begin{pmatrix} -\frac{\sqrt{n(1-\chi_-)}}{\sqrt{n+\chi_-}} |n+1\rangle \\ 0 \\ \frac{\sqrt{(n+1)\chi_-}}{\sqrt{n+\chi_-}} |n-1\rangle \end{pmatrix}, \quad (\text{A9})$$

and

$$|n = 0, F, s = -, k_y\rangle = \frac{e^{ik_y y}}{\sqrt{L_y}} \begin{pmatrix} |0\rangle \\ 0 \\ 0 \end{pmatrix}. \quad (\text{A10})$$

## APPENDIX B: MATRIX ELEMENTS OF VELOCITY OPERATORS

The velocity operators are given by

$$v^x = \frac{i}{\hbar} [H, x] = s v_F \begin{pmatrix} 0 & \cos(\varphi) & 0 \\ \cos(\varphi) & 0 & \sin(\varphi) \\ 0 & \sin(\varphi) & 0 \end{pmatrix}. \quad (\text{B1})$$

The matrix elements of velocity operators are

$$\langle n, \lambda, s, k_y | v^x | n', \lambda', s', k'_y \rangle = \frac{v_F \delta_{ss'} \delta_{k_y k'_y}}{2} \left[ \begin{aligned} & \left( \frac{\lambda'(1-\chi_s)\sqrt{n}}{\sqrt{(n+\chi_s)}} + \frac{\lambda\chi_s\sqrt{n'+1}}{\sqrt{(n'+\chi_s)}} \right) \delta_{n-1, n'} \\ & + \left( \frac{\lambda(1-\chi_s)\sqrt{n'}}{\sqrt{(n'+\chi_s)}} + \frac{\lambda'\chi_s\sqrt{n+1}}{\sqrt{(n+\chi_s)}} \right) \delta_{n+1, n'} \end{aligned} \right], \quad (\text{B2})$$

$$\langle n, \lambda, s, k_y | v^x | n' > 0, F, s', k'_y \rangle = \frac{v_F \delta_{ss'} \delta_{k_y k'_y}}{\sqrt{2}} \left[ \frac{\lambda\sqrt{(1-\chi_s)\chi_s}\sqrt{n'+1}}{\sqrt{(n'+\chi_s)}} \delta_{n+1, n'} - \frac{\lambda\sqrt{(1-\chi_s)\chi_s}\sqrt{n'}}{\sqrt{(n'+\chi_s)}} \delta_{n-1, n'} \right], \quad (\text{B3})$$

and

$$\langle n, \lambda, s, k_y | v^x | n' = 0, F, s', k'_y \rangle = \frac{v_F \delta_{ss'} \delta_{k_y k'_y}}{\sqrt{2}} [\lambda\sqrt{\chi_s} \delta_{n, n'=0}]. \quad (\text{B4})$$

## APPENDIX C: CONDUCTIVITY-THE KUBO-STREDA FORMULA

The conductivity can be calculated using the Kubo-Streda formula [78,79]

$$\sigma_{xx}(E_F) = \int_{-\infty}^{+\infty} d\epsilon \frac{-df_0(\epsilon)}{d\epsilon} \sigma_{xx}(\epsilon), \quad (\text{C1})$$

with

$$\sigma_{xx}(\epsilon) = \frac{e^2 \hbar}{4\pi L^2} Tr \langle v^x A(\epsilon) v^x A(\epsilon) \rangle, \quad (\text{C2})$$

where  $A(\epsilon) = i[G(\epsilon + i\Gamma) - G(\epsilon - i\Gamma)]$ ,  $G(\epsilon \pm i\Gamma) \equiv \frac{1}{\epsilon - H \pm i\Gamma}$ , and  $\Gamma$  characterize the impurity scattering rate (we assume that  $\Gamma$  is constant for simplicity). Calculating the trace with eigenfunctions in Appendix A and matrix elements of velocity operators in Appendix B, we obtain

$$\sigma_{xx}(\epsilon) = \frac{e^2}{h} \frac{1}{8\pi} \frac{2\hbar^2 v_F^2}{l_B^2} \left[ \sum_{n \geq 0, \lambda \lambda', s} \left( \frac{\lambda'(1-\chi_s)\sqrt{n+1}}{\sqrt{(n+1+\chi_s)}} + \frac{\lambda\chi_s\sqrt{n+1}}{\sqrt{(n+\chi_s)}} \right)^2 A_{n,\lambda',s} A_{n+1,\lambda,s} \right. \\ \left. + \sum_{n \geq 0, \lambda F, s} \frac{(1-\chi_s)\chi_s(n+2)}{(n+1+\chi_s)} A_{n+1,F,s} A_{n,\lambda,s} + \sum_{n \geq 1, \lambda F, s} \frac{(1-\chi_s)\chi_s n}{(n+\chi_s)} A_{n,F,s} A_{n+1,\lambda,s} \right. \\ \left. + \sum_{\lambda, s} \chi_s A_{n'=0,F,s} A_{n=0,\lambda,s} \right], \quad (C3)$$

where  $A_{n,\lambda/F,s}(\epsilon) = \frac{2\Gamma}{(\epsilon - E(n,\lambda/F,s,k_y)/E_0)^2 + \Gamma^2}$ . Considering the energy  $\epsilon \rightarrow 0$  and  $n = 0$ , the result is

$$\sigma_{xx}(\epsilon) = C_F^A \frac{\Gamma^2}{\epsilon^2 + \Gamma^2}, \quad (C4)$$

where

$$C_F^A = \frac{e^2}{h} \frac{1}{2\pi} \frac{2\hbar^2 v_F^2}{l_B^2} \left[ 4 + \sum_{n \geq 0, \lambda F, s} \frac{(1-\chi_s)\chi_s(n+2)}{(n+1+\chi_s)} \frac{1}{(\lambda\sqrt{n+\chi_s})^2} \right. \\ \left. + \sum_{n \geq 1, \lambda F, s} \frac{(1-\chi_s)\chi_s n}{(n+\chi_s)} \frac{1}{(\lambda\sqrt{n+1+\chi_s})^2} \right]. \quad (C5)$$

For analytical calculation, we consider the leading order  $C_F^A = \frac{e^2}{h} \frac{2}{\pi} \frac{2\hbar^2 v_F^2}{l_B^2}$ .

- 
- [1] K. S. Novoselov, A. K. Geim, S. V. Morozov, D. Jiang, Y. Zhang, S. V. Dubonos, I. V. Grigorieva, and A. A. Firsov, Electric field effect in atomically thin carbon films, *Science* **306**, 666 (2004).
- [2] M. Z. Hasan and C. L. Kane, *Colloquium*: Topological insulators, *Rev. Mod. Phys.* **82**, 3045 (2010).
- [3] X.-L. Qi and S.-C. Zhang, Topological insulators and superconductors, *Rev. Mod. Phys.* **83**, 1057 (2011).
- [4] N. P. Armitage, E. J. Mele, and A. Vishwanath, Weyl and Dirac semimetals in three-dimensional solids, *Rev. Mod. Phys.* **90**, 015001 (2018).
- [5] B. Bradlyn, J. Cano, Z. Wang, M. G. Vergniory, C. Felser, R. J. Cava, and B. A. Bernevig, Beyond Dirac and Weyl fermions: Unconventional quasiparticles in conventional crystals, *Science* **353**, aaf5037 (2016).
- [6] Z. Lan, N. Goldman, A. Bermudez, W. Lu, and P. Öhberg, Dirac-Weyl fermions with arbitrary spin in two-dimensional optical superlattices, *Phys. Rev. B* **84**, 165115 (2011).
- [7] B. Dóra, J. Kailasvuori, and R. Moessner, Lattice generalization of the Dirac equation to general spin and the role of the flat band, *Phys. Rev. B* **84**, 195422 (2011).
- [8] J. D. Malcolm and E. J. Nicol, Magneto-optics of general pseudospin- $s$  two-dimensional Dirac-Weyl fermions, *Phys. Rev. B* **90**, 035405 (2014).
- [9] D. Leykam, A. Andreanov, and S. Flach, Artificial flat band systems: From lattice models to experiments, *Adv. Phys.: X* **3**, 1473052 (2018).
- [10] Y. Cao, V. Fatemi, S. Fang, K. Watanabe, T. Taniguchi, E. Kaxiras, and P. Jarillo-Herrero, Unconventional superconductivity in magic-angle graphene superlattices, *Nature (London)* **556**, 43 (2018).
- [11] Y. Cao, V. Fatemi, A. Demir, S. Fang, S. L. Tomarken, J. Y. Luo, J. D. Sanchez-Yamagishi, K. Watanabe, T. Taniguchi, E. Kaxiras *et al.*, Correlated insulator behaviour at half-filling in magic-angle graphene superlattices, *Nature (London)* **556**, 80 (2018).
- [12] A. Raoux, M. Morigi, J.-N. Fuchs, F. Piéchon, and G. Montambaux, From dia- to paramagnetic orbital susceptibility of massless fermions, *Phys. Rev. Lett.* **112**, 026402 (2014).
- [13] F. Wang and Y. Ran, Nearly flat band with Chern number  $C = 2$  on the dice lattice, *Phys. Rev. B* **84**, 241103(R) (2011).
- [14] M. Rizzi, V. Cataudella, and R. Fazio, Phase diagram of the Bose-Hubbard model with  $\mathcal{T}_3$  symmetry, *Phys. Rev. B* **73**, 144511 (2006).
- [15] D. Bercioux, D. F. Urban, H. Grabert, and W. Häusler, Massless Dirac-Weyl fermions in a  $\mathcal{T}_3$  optical lattice, *Phys. Rev. A* **80**, 063603 (2009).
- [16] M. Orlita, D. M. Basko, M. S. Zholudev, F. Teppe, W. Knap, V. I. Gavrilenko, N. N. Mikhailov, S. A. Dvoretckii, P. Neugebauer, C. Faugeras *et al.*, Observation of three-dimensional massless Kane fermions in a zinc-blende crystal, *Nat. Phys.* **10**, 233 (2014).
- [17] J. D. Malcolm and E. J. Nicol, Magneto-optics of massless Kane fermions: Role of the flat band and unusual Berry phase, *Phys. Rev. B* **92**, 035118 (2015).
- [18] D. F. Urban, D. Bercioux, M. Wimmer, and W. Häusler, Barrier transmission of Dirac-like pseudospin-one particles, *Phys. Rev. B* **84**, 115136 (2011).
- [19] E. Illes and E. J. Nicol, Klein tunneling in the  $\alpha - \mathcal{T}_3$  model, *Phys. Rev. B* **95**, 235432 (2017).
- [20] Y. Betancur-Ocampo, G. Coudourier-Maruri, V. Gupta, and R. de Coss, Super-Klein tunneling of massive pseudospin-one particles, *Phys. Rev. B* **96**, 024304 (2017).
- [21] X. Feng, Y. Liu, Z.-M. Yu, Z. Ma, L. K. Ang, Y. S. Ang, and S. A. Yang, Super-Andreev reflection and longitudinal shift of pseudospin-1 fermions, *Phys. Rev. B* **101**, 235417 (2020).
- [22] X. Zhou, Andreev reflection and Josephson effect in the  $\alpha - \mathcal{T}_3$  lattice, *Phys. Rev. B* **104**, 125441 (2021).
- [23] W. Zeng and R. Shen, Andreev reflection of massive pseudospin-1 fermions, *New J. Phys.* **24**, 043021 (2022).

- [24] E. Illes, J. P. Carbotte, and E. J. Nicol, Hall quantization and optical conductivity evolution with variable Berry phase in the  $\alpha-T_3$  model, *Phys. Rev. B* **92**, 245410 (2015).
- [25] L. Chen, J. Zuber, Z. Ma, and C. Zhang, Nonlinear optical response of the  $\alpha-T_3$  model due to the nontrivial topology of the band dispersion, *Phys. Rev. B* **100**, 035440 (2019).
- [26] T. Louvet, P. Delplace, A. A. Fedorenko, and D. Carpentier, On the origin of minimal conductivity at a band crossing, *Phys. Rev. B* **92**, 155116 (2015).
- [27] J. Wang, J. F. Liu, and C. S. Ting, Recovered minimal conductivity in the  $\alpha-T_3$  model, *Phys. Rev. B* **101**, 205420 (2020).
- [28] M. Vigh, L. Oroszlány, S. Vajna, P. San-Jose, G. Dávid, J. Cserti, and B. Dóra, Diverging dc conductivity due to a flat band in a disordered system of pseudospin-1 Dirac-Weyl fermions, *Phys. Rev. B* **88**, 161413(R) (2013).
- [29] T. Andrijauskas, E. Anisimovas, M. Račiūnas, A. Mekys, V. Kudriašov, I. B. Spielman, and G. Juzeliūnas, Three-level Haldane-like model on a dice optical lattice, *Phys. Rev. A* **92**, 033617 (2015).
- [30] B. Dey and T. K. Ghosh, Floquet topological phase transition in the  $\alpha-T_3$  lattice, *Phys. Rev. B* **99**, 205429 (2019).
- [31] B. Dey, P. Kapri, O. Pal, and T. K. Ghosh, Unconventional phases in a Haldane model of dice lattice, *Phys. Rev. B* **101**, 235406 (2020).
- [32] J. Wang and J.-F. Liu, Quantum spin Hall phase transition in the  $\alpha-T_3$  lattice, *Phys. Rev. B* **103**, 075419 (2021).
- [33] T. Biswas and T. K. Ghosh, Dynamics of a quasiparticle in the  $\alpha-T_3$  model: Role of pseudospin polarization and transverse magnetic field on Zitterbewegung, *J. Phys.: Condens. Matter* **30**, 075301 (2018).
- [34] D. O. Oriekhov and V. P. Gusynin, RKKY interaction in a doped pseudospin-1 fermion system at finite temperature, *Phys. Rev. B* **101**, 235162 (2020).
- [35] O. Roslyak, G. Gumbs, A. Balassis, and H. Elsayed, Effect of magnetic field and chemical potential on the RKKY interaction in the  $\alpha-T_3$  lattice, *Phys. Rev. B* **103**, 075418 (2021).
- [36] L. Tamang and T. Biswas, Probing topological signatures in an optically driven  $\alpha-T_3$  lattice, *Phys. Rev. B* **107**, 085408 (2023).
- [37] L. Tamang, T. Nag, and T. Biswas, Floquet engineering of low-energy dispersions and dynamical localization in a periodically kicked three-band system, *Phys. Rev. B* **104**, 174308 (2021).
- [38] M. A. Mojarro, V. G. Ibarra-Sierra, J. C. Sandoval-Santana, R. Carrillo-Bastos, and G. G. Naumis, Electron transitions for Dirac Hamiltonians with flat bands under electromagnetic radiation: Application to the  $\alpha-T_3$  graphene model, *Phys. Rev. B* **101**, 165305 (2020).
- [39] A. Iurov, G. Gumbs, and D. Huang, Peculiar electronic states, symmetries, and Berry phases in irradiated  $\alpha-T_3$  materials, *Phys. Rev. B* **99**, 205135 (2019).
- [40] B. Dey and T. K. Ghosh, Photoinduced valley and electron-hole symmetry breaking in  $\alpha-T_3$  lattice: The role of a variable berry phase, *Phys. Rev. B* **98**, 075422 (2018).
- [41] H.-Y. Xu, L. Huang, D. Huang, and Y.-C. Lai, Geometric valley Hall effect and valley filtering through a singular Berry flux, *Phys. Rev. B* **96**, 045412 (2017).
- [42] F. Bouhadida, L. Mandhour, and S. Charfi-Kaddour, Magnetic Fabry-Pérot interferometer for valley filtering in a honeycomb-dice model, *Phys. Rev. B* **102**, 075443 (2020).
- [43] Z. P. Niu and S. J. Wang, Valley polarized transport and negative differential resistance in an irradiated  $\alpha-T_3$  lattice, *J. Phys. D* **55**, 255303 (2022).
- [44] A. Filusch, A. R. Bishop, A. Saxena, G. Wellein, and H. Fehske, Valley filtering in strain-induced  $\alpha-T_3$  quantum dots, *Phys. Rev. B* **103**, 165114 (2021).
- [45] D. Huang, A. Iurov, H.-Y. Xu, Y.-C. Lai, and G. Gumbs, Interplay of Lorentz-Berry forces in position-momentum spaces for valley-dependent impurity scattering in  $\alpha-T_3$  lattices, *Phys. Rev. B* **99**, 245412 (2019).
- [46] S.F. Islam and P. Dutta, Valley-polarized magnetoconductivity and particle-hole symmetry breaking in a periodically modulated  $\alpha-T_3$  lattice, *Phys. Rev. B* **96**, 045418 (2017).
- [47] O. V. Bugaiko and D. O. Oriekhov, Electronic states of pseudospin-1 fermions in  $\alpha-T_3$  lattice ribbons in a magnetic field, *J. Phys.: Condens. Matter* **31**, 325501 (2019).
- [48] Y. Xu and L.-M. Duan, Unconventional quantum Hall effects in two-dimensional massive spin-1 fermion systems, *Phys. Rev. B* **96**, 155301 (2017).
- [49] J. J. Wang, S. Liu, J. Wang, and J.-F. Liu, Integer quantum Hall effect of the  $\alpha-T_3$  model with a broken flat band, *Phys. Rev. B* **102**, 235414 (2020).
- [50] T. Biswas and T. K. Ghosh, Magnetotransport properties of the  $\alpha-T_3$  model, *J. Phys.: Condens. Matter* **28**, 495302 (2016).
- [51] E. Illes and E. J. Nicol, Magnetic properties of the  $\alpha-T_3$  model: Magneto-optical conductivity and the Hofstadter butterfly, *Phys. Rev. B* **94**, 125435 (2016).
- [52] Y.-R. Chen, Y. Xu, J. Wang, J.-F. Liu, and Z. Ma, Enhanced magneto-optical response due to the flat band in nanoribbons made from the  $\alpha-T_3$  lattice, *Phys. Rev. B* **99**, 045420 (2019).
- [53] A. D. Kovács, G. Dávid, B. Dóra, and J. Cserti, Frequency-dependent magneto-optical conductivity in the generalized  $\alpha-T_3$  model, *Phys. Rev. B* **95**, 035414 (2017).
- [54] C.-Z. Wang, H.-Y. Xu, and Y.-C. Lai, Super skew scattering in two-dimensional Dirac material systems with a flat band, *Phys. Rev. B* **103**, 195439 (2021).
- [55] E. V. Gorbar, V. P. Gusynin, and D. O. Oriekhov, Electron states for gapped pseudospin-1 fermions in the field of a charged impurity, *Phys. Rev. B* **99**, 155124 (2019).
- [56] X. Ye, S.-S. Ke, X.-W. Du, Y. Guo, and H.-F. Lü, Quantum tunneling in the  $\alpha-T_3$  model with an effective mass term, *J. Low Temp. Phys.* **199**, 1332 (2020).
- [57] E. V. Gorbar, V. P. Gusynin, and D. O. Oriekhov, Gap generation and flat band catalysis in dice model with local interaction, *Phys. Rev. B* **103**, 155155 (2021).
- [58] N. Weekes, A. Iurov, L. Zhemchuzhna, G. Gumbs, and D. Huang, Generalized WKB theory for electron tunneling in gapped  $\alpha-T_3$  lattices, *Phys. Rev. B* **103**, 165429 (2021).
- [59] S. M. Cunha, D. R. da Costa, J. M. Pereira, Jr., R. N. C. Filho, B. Van Duppen, and F. M. Peeters, Tunneling properties in  $\alpha-T_3$  lattices: Effects of symmetry-breaking terms, *Phys. Rev. B* **105**, 165402 (2022).
- [60] A. Singh and G. Sharma, Geometrical transport in pseudospin-1 fermions, *Phys. Rev. B* **107**, 245150 (2023).
- [61] J. Sun, T. Liu, Y. Du, and H. Guo, Strain-induced pseudomagnetic field in  $\alpha-T_3$  lattice, *Phys. Rev. B* **106**, 155417 (2022).
- [62] M. W. Alam, B. Souayah, and S. F. Islam, Enhancement of thermoelectric performance of a nanoribbon made of  $\alpha-T_3$  lattice, *J. Phys.: Condens. Matter* **31**, 485303 (2019).

- [63] Y. Xing, Q. F. Sun, and J. Wang, Nernst and Seebeck effects in a graphene nanoribbon, *Phys. Rev. B* **80**, 235411 (2009).
- [64] J. G. Checkelsky and N. P. Ong, Thermopower and Nernst effect in graphene in a magnetic field, *Phys. Rev. B* **80**, 081413(R) (2009).
- [65] Y. M. Zuev, W. Chang, and P. Kim, Thermoelectric and magnetothermoelectric transport measurements of graphene, *Phys. Rev. Lett.* **102**, 096807 (2009).
- [66] P. Wei, W. Bao, Y. Pu, C. N. Lau, and J. Shi, Anomalous thermoelectric transport of Dirac particles in graphene, *Phys. Rev. Lett.* **102**, 166808 (2009).
- [67] L. Zhu, R. Ma, L. Sheng, M. Liu, and D.-N. Sheng, Universal thermoelectric effect of Dirac Fermions in graphene, *Phys. Rev. Lett.* **104**, 076804 (2010).
- [68] W. Duan, J. Liu, C. Zhang, and Z. Ma, The magnetothermoelectric effect of graphene with intra-valley scattering, *Chin. Phys. B* **27**, 097204 (2018).
- [69] W. Duan, J.-F. Liu, C. Zhang, and Z. Ma, Thermoelectric and thermal transport properties of graphene under strong magnetic field, *Phys. E* **104**, 173 (2018).
- [70] M. Jonson and S. M. Girvin, Thermoelectric effect in a weakly disordered inversion layer subject to a quantizing magnetic field, *Phys. Rev. B* **29**, 1939 (1984).
- [71] H. Oji and P. Streda, Theory of electronic thermal transport: Magnetoquantum corrections to the thermal transport coefficients, *Phys. Rev. B* **31**, 7291 (1985).
- [72] W. Long, H. Zhang, and Q. F. Sun, Quantum thermal Hall effect in graphene, *Phys. Rev. B* **84**, 075416 (2011).
- [73] M. P. L. Sancho, J. M. L. Sancho, J. M. L. Sancho, and J. Rubio, Highly convergent schemes for the calculation of bulk and surface Green functions, *J. Phys. F: Met.* **15**, 851 (1985).
- [74] S. Datta, Nanoscale device modeling: The Green's function method, *Superlattices Microstruct.* **28**, 253 (2000).
- [75] S. Datta, *Quantum Transport: Atom to Transistor* (Cambridge University Press, New York, 2005).
- [76] D. Ryndyk, *Theory of Quantum Transport at Nanoscale* (Springer, Cham, 2016).
- [77] K. Behnia, *Fundamentals of Thermoelectricity* (Oxford University Press, New York, 2015).
- [78] P. Štředa and L. Smrčka, Galvanomagnetic effects in alloys in quantizing magnetic fields, *Phys. Status Solidi (b)* **70**, 537 (1975).
- [79] N. H. Shon and T. Ando, Quantum transport in two-dimensional graphite system, *J. Phys. Soc. Jpn.* **67**, 2421 (1998).